Small Structures

www.small-structures.com

RESEARCH ARTICLE OPEN ACCESS

Strain-Induced Piezo-Optoelectronic Coupling in Monolayer MoS_2

Ajay Kumar Verma[1,2] | Pargam Vashishtha[3] | Vishnu Aggarwal[1] | Boopathiraja Kanan[1] | Sindhu P. Giridhar[1] | Tanish Gupta[1] | Md. Ataur Rahman[4] | Manoj Sehrawat[1] | Chenglong Xu[5] | Billy J. Murdoch[6] | Edwin L. H. Mayes[6] | S. R. Dhakate[7,8] | Bhasker Gahtori[7,8] | Taimur Ahmed[1] | Irfan H. Abidi[1] | Sumeet Walia[1]

[1]Centre for Opto-electronic Materials and Sensors (COMAS), School of Engineering, RMIT University, Melbourne, Australia | [2]Light Technology Institute, Karlsruhe Institute of Technology (KIT), Karlsruhe, Germany | [3]Department of Electrical and Computer Engineering, University of Wisconsin–Madison, Madison, Wisconsin, USA | [4]Functional Materials and Microsystems Research Group and the Micro Nano Research Facility, RMIT University, Melbourne, Australia | [5]Micro Nano Research Facility, RMIT University, Melbourne, Australia | [6]RMIT Microscopy and Microanalysis Facility, RMIT University, Melbourne, Australia | [7]CSIR-National Physical Laboratory, New Delhi, India | [8]Academy of Scientific & Innovative Research (AcSIR), Ghaziabad, India

Correspondence: Irfan H. Abidi (irfan.haider.abidi@rmit.edu.au) | Sumeet Walia (sumeet.walia@rmit.edu.au)

Received: 19 September 2025 | **Revised:** 19 November 2025 | **Accepted:** 8 December 2025

Keywords: 2D materials | monolayer MoS_2 | optoelectronic | PFM | piezoelectric | TMDs

ABSTRACT

Piezo-optoelectronic coupling, the direct modulation of photoresponse by strain-induced piezoelectric polarization, is a theoretically promising route to adaptive, programmable optoelectronics, yet it remains experimentally elusive in scalable two-dimensional systems. Here, we present large-area monolayer MoS_2 as a robust platform for probing and controlling this coupling at the atomic limit, and a single device made on it demonstrates integrated functionality for energy generation, strain sensing, and photodetection within a unified configuration. Using dual AC resonance tracking piezoresponse force microscopy, we quantify an out-of-plane piezoelectric coefficient ($d_{33}^{\text{eff}} = 0.64$ pm/V) and demonstrate a pronounced, strain-tunable internal piezoelectric polarization that enables exciton dissociation under low bias and illumination, distinct from conventional photodetection approaches. While absolute responsivity is modest, the observed strain-induced enhancement of photocurrent and the clear correlation with measured piezoresponse reveal that mechanical deformation can be leveraged as a precise control knob for charge separation and light–matter interaction in ultrathin semiconductors. These findings provide direct experimental insight into piezo-optoelectronic coupling, establishing monolayer MoS_2 as a multifunctional and scalable platform for future studies of coupled electromechanical photonic phenomena and for the development of programmable optoelectronics, hybrid sensors, and next-generation flexible devices.

1 | Introduction

Piezo-optoelectronic coupling, the direct modulation of optical properties through strain-induced piezoelectric fields, represents a fundamental mechanism for controlling light–matter interactions in semiconductors [1, 2]. While theoretical predictions suggest this coupling could enable programmable optoelectronics with mechanical tunability, experimental demonstration remains challenging, particularly in atomically thin materials where quantum confinement effects and reduced screening amplify electromechanical responses [3, 4].

Two-dimensional (2D) materials offer an ideal platform for investigating piezo-optoelectronic phenomena due to their atomic-scale thickness, broken inversion symmetry (in odd-layer systems), and strong strain-dependent electronic properties [5–8]. Transition metal dichalcogenides (TMDs) like monolayer MoS_2 exhibit intrinsic piezoelectricity absent in their bulk counterparts due to the loss of centrosymmetry in the monolayer limit [9–11]. Simultaneously, these materials display strong excitonic effects and efficient light–matter coupling, making them promising candidates for strain-tunable optoelectronics [12–15].

This is an open access article under the terms of the Creative Commons Attribution License, which permits use, distribution and reproduction in any medium, provided the original work is properly cited.

© 2026 The Author(s). *Small Structures* published by Wiley-VCH GmbH.

https://doi.org/10.1002/sstr.202500657

However, experimental verification of coupled piezoelectric–optoelectronic behavior faces several challenges. First, distinguishing strain-induced piezoelectric effects from conventional piezoresistive responses requires precise measurement of both mechanical deformation and corresponding changes in charge transport [16]. Second, the magnitude of piezoelectric coefficients in 2D materials is often small compared to bulk ferroelectrics, demanding sensitive characterization techniques [17]. Third, most studies have investigated piezoelectric and optoelectronic properties separately, leaving the fundamental coupling mechanisms unexplored [18, 19].

While individual studies have demonstrated piezoelectric energy harvesting [18, 20–22] and strain-tunable photoconductivity [23, 24] in 2D materials, the correlation between strain-induced polarization fields and photoresponse modulation, the essence of piezo-optoelectronic coupling, and the development of multifunctional devices remain largely unexplored. Wu et al. have first experimentally realized the piezoelectricity in monolayer MoS_2; they made a flexible piezoelectric device (PED) which converted mechanical energy into an electrical signal [15]. Gant et al. have fabricated a simple flexible photodetector using a MoS_2 monolayer and showed the change in photoresponse due to the strain generated by thermal treatment [23]. Wu et al. demonstrated photocurrent modulation in a strain-gated MoS_2 monolayer-based flexible phototransistor [25]. Despite these advances, a critical gap persists regarding how mechanical deformation can be harnessed as a direct control parameter in optoelectronic devices, thereby limiting progress toward mechanically programmable, strain-tunable photonic systems. Furthermore, expanding the functionality of MoS_2 monolayer-based devices beyond conventional photodetectors toward integrated energy generation, sensing, and photodetection would represent a significant step toward next-generation multifunctional flexible electronics.

In this work, we provide direct experimental evidence of piezo-optoelectronic coupling in large-area monolayer MoS_2 through correlated piezoelectric and photoresponse measurements. Using dual AC resonance tracking piezoresponse force microscopy (DART-PFM), we quantify the out-of-plane piezoelectric coefficient ($d_{33}^{\mathrm{eff}} = 0.64\,\mathrm{pm/V}$) and demonstrate strain-tunable internal piezoelectric polarization that dramatically enhances photoresponse under tensile strain. Our device exhibits negligible photocurrent in the unstrained state but generates 40 nA under combined optical illumination (565 nm, 20 $\mathrm{mW/cm^2}$) and tensile strain (1.2%) at 1 V bias. This strain-dependent photoresponse correlates directly with the measured piezoelectric activity, revealing a clear mechanism in which the strain-induced polarization field acts as a driving force for exciton dissociation and charge separation. These findings advance the fundamental understanding of electromechanical optical coupling in atomically thin semiconductors and establish the design principles for multifunctional MoS_2-based flexible devices capable of energy harvesting, sensing, and photodetection.

2 | Results and Discussion

Figure 1a shows a schematic of the two-temperature-zone chemical vapor deposition (CVD) system used to synthesize monolayer MoS_2 crystals under low pressure. In this setup, sulfur powder is vaporized at 180°C in zone 1, and an inert argon gas carries the resulting sulfur vapor into zone 2, where the MoO_3 powder, a precursor for molybdenum, reacts on a substrate to grow a continuous monolayer MoS_2 film (details can be found in the Experimental Section 4.1). Below the schematic, an atomic model illustrates the structure of the as-grown monolayer MoS_2 film.

Figure 1b shows optical microscopy images of the as-grown monolayer MoS_2 on 300 nm SiO_2/Si substrate, highlighting its continuous and uniform growth over a large area. The transferred MoS_2 monolayer on a gold substrate was characterized by atomic force microscopy (AFM), and its height profile is presented in Figure 1c. The measured thickness of ~0.7 nm confirms the monolayer nature of the crystal, consistent with previous reports for single-layer MoS_2 [20, 26]. Figure 1d shows the corresponding AFM phase map of the same region.

To further investigate the atomic-scale features of the MoS_2 monolayer, high-resolution transmission electron microscopy (HRTEM) was performed. Figure 1e displays an HRTEM image of a representative area of the monolayer. The selected area electron diffraction (SAED) pattern is presented in Figure 1f, which confirms the crystallographic orientation of the MoS_2 monolayer in reciprocal space. A magnified view of the selected region (R1) in Figure 1g reveals clear lattice fringes with interplanar distances of ~0.27 and ~0.16 nm, corresponding to the (100) and (110) planes of MoS_2, respectively. A few point defects, likely sulfur vacancies, are visible and marked with blue arrows.

To further assess the optical characteristics of the monolayer MoS_2, Raman and photoluminescence (PL) spectroscopy were employed. Figure 2a shows the Raman spectra of the MoS_2 crystal, whereby the $E^1{}_{2g}$ and A_{1g} peaks correspond to the in-plane and out-of-plane vibrational modes of MoS_2, respectively. The peaks $E^1{}_{2g}$ and A_{1g} were observed at 382.5 and 403.3 $\mathrm{cm^{-1}}$, respectively, with a frequency variance of 20.8 $\mathrm{cm^{-1}}$, which closely aligns with the reported value for a monolayer MoS_2 [27, 28]. Figure 2b depicts the PL spectrum, showing a pronounced A-excitonic peak at 1.82 eV, accompanied by a weaker B-excitonic peak at 1.98 eV. These excitonic resonances correspond to direct transitions at the K-point of the Brillouin zone, where spin–orbit splitting in the valence band (VB) accounts for the energy difference between them [29]. The intensity and sharpness of the A-exciton peak serve as indicators of the crystal's optical quality, confirming that the monolayer grown here is of high purity and minimal defect density [27, 30].

To get more information about chemical states and compositional information, X-ray photoelectron spectroscopy (XPS) experiment was executed using a surface-sensitive probe at 1486.7 eV soft X-rays. The experimental results of Mo 3d states are shown in Figure 2c, which shows the characteristic doublet corresponding to Mo^{4+} 3d and Mo^{6+} 3d states. Mo^{4+} 3d doublets were observed at 229.45 eV (Mo^{4+} $3d_{5/2}$) and 232.55 eV (Mo^{4+} $3d_{3/2}$). Also, MoO_x-related peaks were observed for Mo^{6+} $3d_{5/2}$ and Mo^{6+} $3d_{3/2}$ states [31]. In the XPS fitting of Mo $3d_{5/2}$ and Mo $3d_{3/2}$, we applied constraints for peak position separation ~3.1 eV, peak ratio of 3/2, and set an equal full width at half maximum (FWHM) for both peaks. Figure 2d exhibits the spectra of S 2p states, where S $2p_{3/2}$ and S $2p_{1/2}$ peaks were detected at 162.4 and 163.6 eV, respectively. To complement this, the VB photoemission spectrum (Figure 2e) reveals a VB onset at 0.98 eV below the Fermi level, confirming the electronic structure near the VB edge. Based on combined PL and XPS data, Figure 2f presents a schematic energy band diagram for the MoS_2 monolayer. The bandgap is determined to be 1.82 eV,

26884062, 2026, 1, Downloaded from https://onlinelibrary.wiley.com/doi/10.1002/sstr.202500657, Wiley Online Library on [12/02/2026]. See the Terms and Conditions (https://onlinelibrary.wiley.com/terms-and-conditions) on Wiley Online Library for rules of use; OA articles are governed by the applicable Creative Commons License

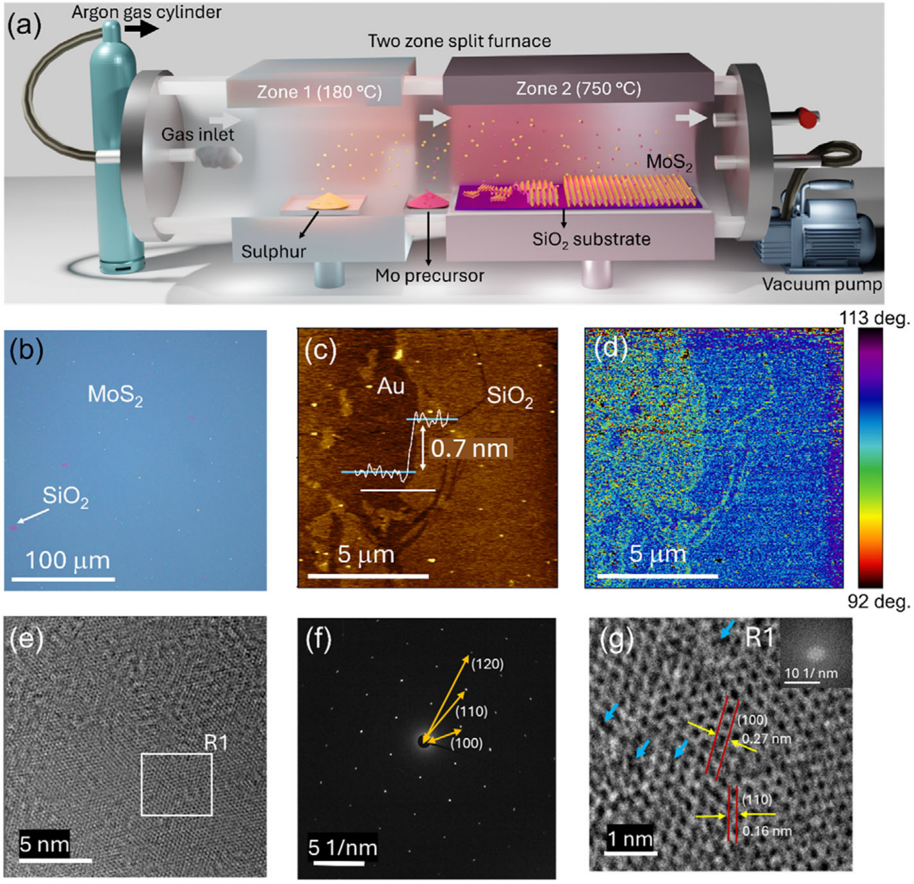

FIGURE 1 | (a) Schematic of utilized CVD processes and the atomic representation of monolayer MoS_2 crystal, (b) the optical image of as-grown MoS_2 crystal over a large area, (c,d) the AFM height profile and phase profile of the transferred MoS_2 monolayer crystal on Au substrate, respectively, (e) the HRTEM image of monolayer crystal, (f) the corresponding SAED pattern, and (g) the magnified view of region R1 of (e), where blue arrows show the defects in the crystal.

with the Fermi level positioned 0.98 eV above the VB maximum, slightly shifted toward the conduction band, indicating an intrinsic n-type nature of the crystal. Further, the elemental mapping of Mo 3d states and survey spectra of the sample has been performed and shown in Figure S1.

To evaluate the sample's work function, scanning Kelvin probe force microscopy (SKPFM) was performed after transferring the MoS_2 monolayer onto a gold substrate [32, 33]. Figure 2g shows a potential map that differentiates the region between MoS_2 and Au substrate, where the measured surface potential shows the contact potential difference (CPD) between the tip and the sample. The measured V_{CPD} is 0.55 and 0.39 eV on MoS_2 and Au, respectively. So the work function Φ for the MoS_2 monolayer was calculated employing the V_{CPD} equation [34, 35]:

$$\Phi_{\text{sample}} = \Phi_{\text{tip}} - eV_{\text{CPD}}$$

The detailed calculation of the work function is showcased in the Supporting Information. The work function of monolayer MoS_2 is calculated to be 4.95 eV, consistent with reported values for monolayer MoS_2 [11]. Figure 2h shows the current map of the monolayer MoS_2 on the gold substrate evaluated by conductive AFM, suggesting a relatively less conducting nature of the MoS_2 crystal compared to the Au substrate. To understand the electrical behavior, field-effect transistor (FET) devices were fabricated from the large-area MoS_2 monolayer [36, 37]. The electrical characterizations were conducted at ambient conditions using a Keithley 4200-SCS. Figure 2i presents FET transfer characteristics of I_{DS}-V_{GS} for the fabricated device at a constant drain to source voltage (V_{DS}) = 3V. The threshold voltage (V_{TH}) was extracted from the slope of the maximum transconductance and found to be approximately 15.38V [38]. The carrier density (n_e) was calculated under identical conditions ($V_{GS} = 30$V and $V_{DS} = 3$V) by employing the relationship [29]; $n_e = (C_{ox}|V_{GS} - V_{TH}|)/e$, where $C_{ox} = 1.15 \times 10^{-8}\ \text{F cm}^{-2}$ is the measured gate oxide capacitance per unit area of dielectrics ($C_{ox} = \varepsilon_0\varepsilon_r/d$; $\varepsilon_r = 3.9$ is for SiO_2, $d = 300$ nm is the thickness of insulating SiO_2 layer), and e is electronic charge $= 1.6 \times 10^{-19}$ C. Thus, the calculated n_e is $1.05 \times 10^{12}\ \text{cm}^{-2}$. The mobility of the carrier has been calculated using the relation [39]:

$$\mu_e = \frac{\Delta I_{DS}}{\Delta V_{GS}} \times \frac{L}{W \times C_{ox} \times V_{DS}}$$

Here, $\frac{\Delta I_{DS}}{\Delta V_{GS}} = 9.97 \times 10^{-10}\ \text{AV}^{-1}$ is the slope of I_{DS} vs. V_{GS} at constant $V_{DS} = 3$V. W and L are the width and length of the channel, and their values were 2.58×10^{-6} and 9.03×10^{-6} m, respectively. Further, the on–off ratio was calculated to be 681, indicating excellent FET performance.

To investigate the electromechanical response of the monolayer MoS_2, PFM was performed using the DART mode. This technique

26884062, 2026, 1, Downloaded from https://onlinelibrary.wiley.com/doi/10.1002/sstr.202500657, Wiley Online Library on [12/02/2026]. See the Terms and Conditions (https://onlinelibrary.wiley.com/terms-and-conditions) on Wiley Online Library for rules of use; OA articles are governed by the applicable Creative Commons License

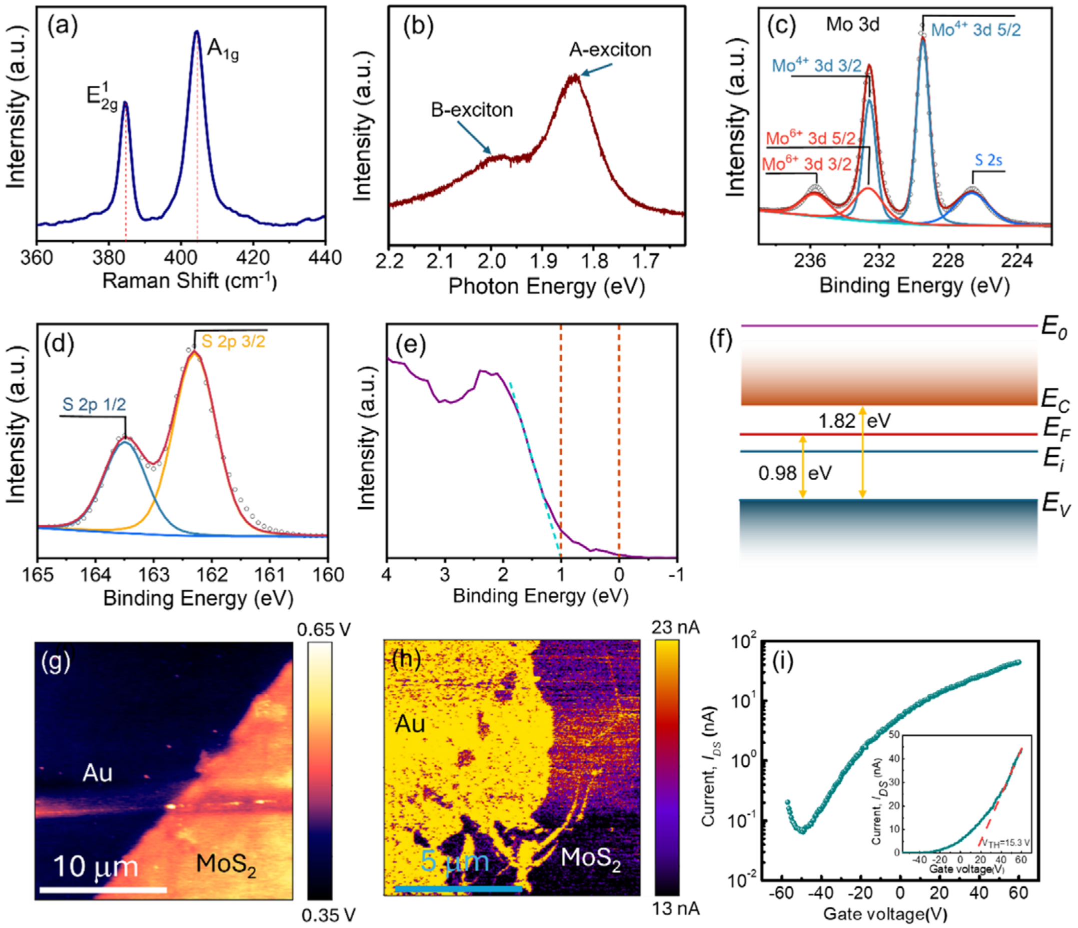

FIGURE 2 | The structural characterization results of the MoS$_2$ crystal. (a) The Raman spectra, (b) PL data, (c–e) the XPS spectra of Mo 3d state, S 2p state, and VB, respectively, (f) schematic of energy band diagram using this data, (g) the surface potential map of the monolayer MoS$_2$ transferred on Au, (h) the current map of the MoS$_2$ monolayer on Au substrate, and (i) the FET characteristics (drain current vs. gate to source voltage plot on logarithmic scale at constant $V_{DS} = 3$ V drain to source voltage) of MoS$_2$ monolayer crystal. Inset shows the drain current vs. gate to source voltage plot on linear scale.

minimizes frequency-dependent phase variations typically caused by cantilever dynamics, enabling more reliable detection of piezoelectric signals in atomically thin materials [11, 40]. A Pt-Ir-coated stiff cantilever with a high spring constant (42 N/m) and short length (160 µm) was employed to reduce electrostatic contributions to the measured piezo amplitude. Additionally, a DC tip bias matching the surface potential was applied to suppress residual electrostatic effects further [16, 41]. PFM measurements were carried out across a range of AC drive voltages from 0 to 4 V. Figure 3a–d shows the piezo amplitude images acquired at 0, 1, 2, and 4 V AC drive voltages, respectively. A progressive increase in the piezo amplitude signal with increasing AC bias was observed, confirming the voltage-dependent piezoelectric response of the monolayer MoS$_2$. The corresponding phase images are provided in Figure S2. To quantify the effective piezoelectric coefficient d_{33}^{eff}, the average piezo amplitude was plotted against the applied AC voltage, as shown in Figure 3e. The achieved out-of-plane piezoelectric coefficient was d_{33}^{eff} 0.64 pm/V for monolayer MoS$_2$.

To evaluate the practical applicability of the synthesized monolayer MoS$_2$ crystal, we fabricated a flexible PED. The device architecture and fabrication procedure are detailed in the Experimental Section and schematically illustrated in Figure S3. The PED is encapsulated with a 0.3-mm-thick insulating layer of PDMS, provides protection from external electrostatic disturbances, and facilitates uniform stress distribution during mechanical actuation. The energy harvesting capabilities of the device were tested through a series of electromechanical experiments, including continuous finger tapping, capacitor charging, and under a commercial mechanical system. Figure 4a shows the schematic of charge generation on finger tapping in the PED. The inset shows a photograph of the actual fabricated device. The mechanism of piezoelectric response upon continuous finger tapping is shown in Figure S4. Figure 4b displays the open-circuit voltage during repeated finger tapping, where a peak-to-peak voltage of ~0.7 V was recorded. The observed voltage peaks correspond to the generation of piezoelectric polarization charges under out-of-plane compressive stress. Distinct upward voltage spikes upon pressing and downward spikes upon releasing are attributed to the generation and relaxation of dipole moments, respectively [42]. To confirm that the output originates from the MoS$_2$ layer, measurements on a blank device without MoS$_2$ were conducted, yielding negligible voltage output (Figure S5a). Figure 4c shows the output current measured across a 2.2 MΩ resistor by this PED on continuous finger tapping. The device generated a maximum average output current of ~50 nA, corresponding to a power output of ~5.5 nW, which is notably higher than that reported for small-area monolayer MoS$_2$-based PEDs [11].

26884062, 2026, 1, Downloaded from https://onlinelibrary.wiley.com/doi/10.1002/sstr.202500657, Wiley Online Library on [12/02/2026]. See the Terms and Conditions (https://onlinelibrary.wiley.com/terms-and-conditions) on Wiley Online Library for rules of use; OA articles are governed by the applicable Creative Commons License

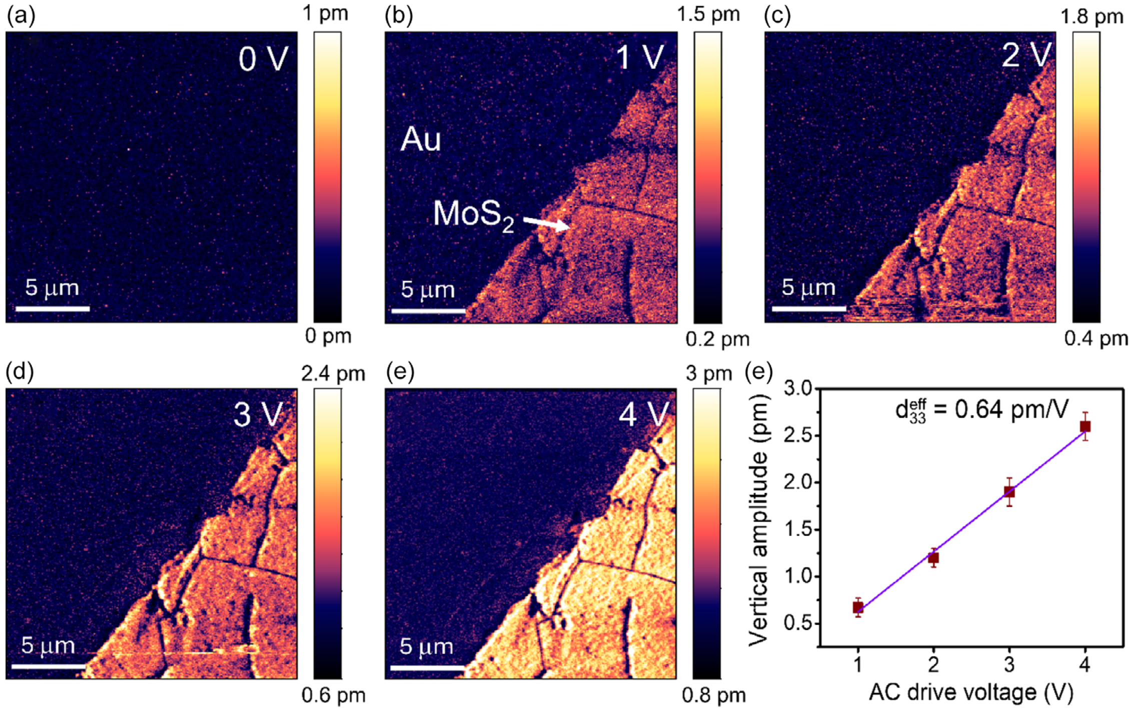

FIGURE 3 | Piezoresponse data of MoS_2 monolayer sample transferred on Au. (a–e) The vertical piezoresponse on AC drive voltage 0, 1, 2, 3, and 4 V, respectively, and (f) the slope of piezoresponse vs. drive voltage to calculate the effective piezoelectric coefficient, which is 0.64 pm/V.

The corresponding voltage output across the load is shown in Figure S5b. To demonstrate energy storage potential, the alternating output was rectified using a full-wave bridge circuit (Figure 4d), yielding an average rectified voltage of ~0.6 V (see extended data in Figure S5c). The rectified output was further utilized to charge capacitors. Figure 4e presents the schematic of the rectification and capacitor-charging setup. As shown in Figure 4f, the PED successfully charged a 440 nF capacitor to ~27 mV under continuous finger tapping. The inset displays a zoomed-in view of the charging profile, revealing a rise time of ~1.2 s. Additionally, the device was capable of charging a 1 µF capacitor up to 35 mV (Figure S5d). These results suggest that the PED can potentially power low-power portable electronics by harvesting mechanical energy from human activities.

To further evaluate the robustness of the device under controlled mechanical stimuli, we utilized a commercial electromechanical vibration system (ElectroPuls E3000) at various frequencies. The schematic and real measurement setups are provided in Figure S6a,b. Figure 4g shows the open-circuit voltage response at a vibration frequency of 5 Hz with a tapping amplitude of 1 mm, where a peak-to-peak voltage of ~1.0 V was observed. At 10 Hz and the same amplitude, the peak-to-peak output voltage increased slightly to ~1.2 V (Figure 4h). The PED also exhibited stable voltage output (~1 V) at 2 Hz, as shown in Figure S6d. Notably, in previously reported MoS_2 monolayer-based piezoelectric nanogenerators, output voltages have ranged from 30 mV to 1.2 V [15, 29, 43]. The higher and more stable open-circuit voltages achieved with our large-area MoS_2 monolayer-based PED underscore its superior piezoelectric performance and its strong potential for real-world energy harvesting applications.

To explore the modulation of photoresponse through strain-induced piezoelectric polarization and to evaluate the multifunctional capabilities of large-area monolayer MoS_2, the same flexible device was tested for its optoelectronic performance under mechanical strain. Figure 5a illustrates the schematic of the measurement configuration, where bending introduces an in-plane tensile strain of approximately 1.2%, calculated using an established method from the literature [44]. This strain changes the electronic band structure of the MoS_2 monolayer and decreases the energy of VB maxima and conduction band minima, thereby improving the light absorption [25]. The mechanical deformation generates an internal piezoelectric field, which facilitates excitation and charge separation upon light illumination, thereby enabling strain-driven piezo-optoelectronic coupling (schematically shown in Figure S7). The inset of Figure 5a shows the actual flexible device used for the measurements. Transient photoresponse(*I*–*t*) measurements were performed using monochromatic light sources with wavelengths of 565 and 660 nm under two external bias voltages (0.5 and 1 V) at an incident light intensity of 20 mW/cm^2. The excitons aquire high binding energy in monolayer and bilayer MoS_2 (150–200 meV) [45]. Therefore, a few kV/cm of an in-plane external electric field is required to separate these excitons [45]. In our device geometry, with a 100 µm electrode spacing, such fields would necessitate tens of volts. Remarkably, by utilizing the built-in piezoelectric polarization generated under mechanical strain, we were able to achieve significant photoresponse at much lower external applied voltages (0.5–1 V), enabled by the strain-induced piezoelectric polarization field, demonstrating effective strain-driven piezo-optoelectronic coupling. This observed behavior is distinct from the photoflexoelectric effect, which arises from strain gradients that induce electric polarization even in nonpiezoelectric materials [46]. In our case, the enhancement originates from uniform strain applied to the intrinsically piezoelectric MoS_2 monolayer, confirming the coupling between piezoelectric polarization and photoresponse

26884062, 2026, 1, Downloaded from https://onlinelibrary.wiley.com/doi/10.1002/sstr.202500657, Wiley Online Library on [12/02/2026]. See the Terms and Conditions (https://onlinelibrary.wiley.com/terms-and-conditions) on Wiley Online Library for rules of use; OA articles are governed by the applicable Creative Commons License

26884062, 2026, 1, Downloaded from https://onlinelibrary.wiley.com/doi/10.1002/sstr.202500657, Wiley Online Library on [12/02/2026]. See the Terms and Conditions (https://onlinelibrary.wiley.com/terms-and-conditions) on Wiley Online Library for rules of use; OA articles are governed by the applicable Creative Commons License

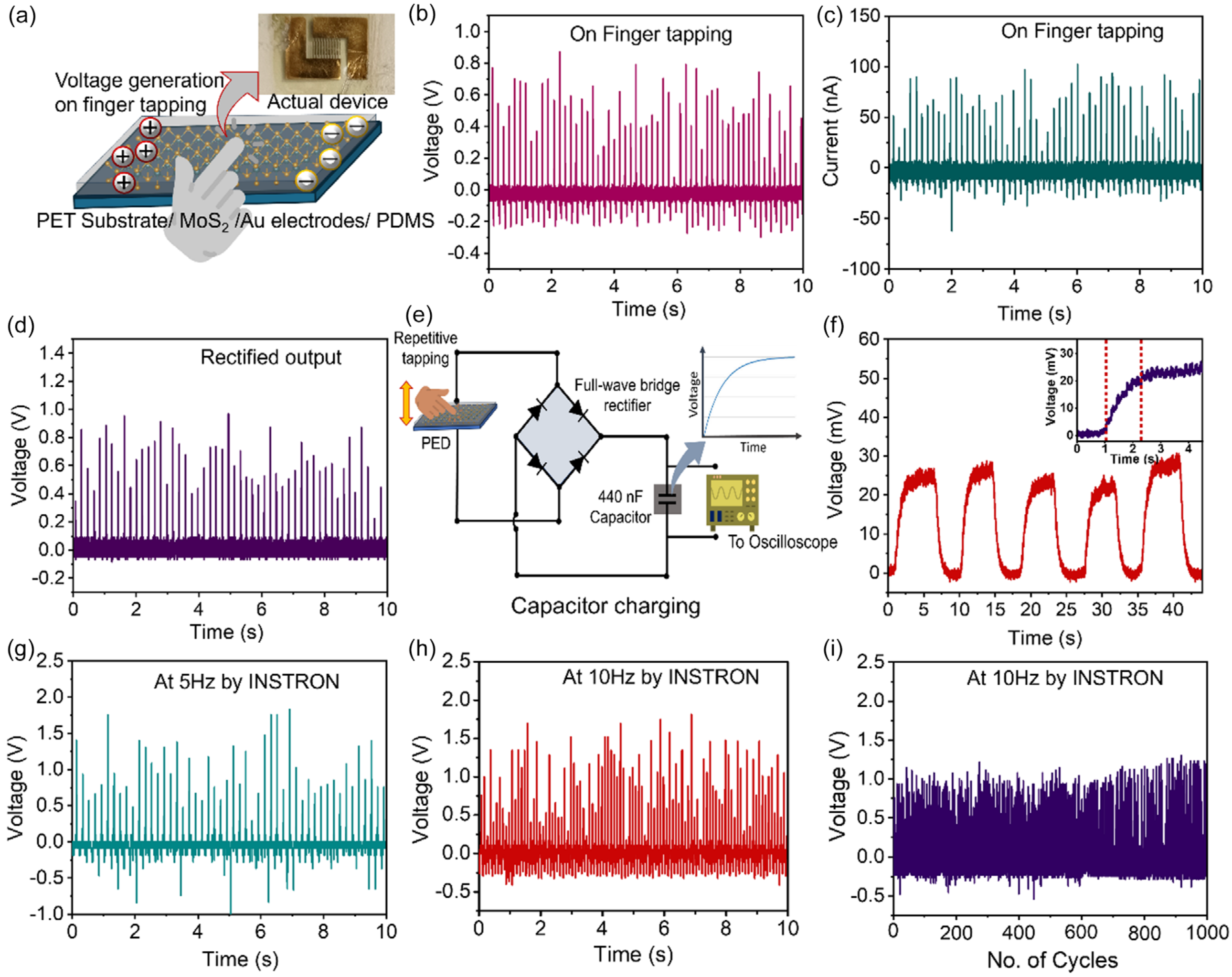

FIGURE 4 | Energy generation by PEDs based on monolayer MoS_2. (a) The schematic voltage generation upon finger tapping; the inset shows the real flexible device. (b) Output voltage on finger tapping. (c) Output current on finger tapping across 2.2 MW resistance. (d) The rectified output voltage on finger tapping using full wave bridge rectifier. (e) The schematic of lab made setup for voltage rectification and capacitor charging. (f) The 440 nF capacitor charging by the finger tapping on PED; the inset figure shows the magnified view of charging. (g–i) The voltage generation by the PED under a commercial mechanical vibration setup INSTRON ElectroPuls E3000: (g) the output voltage at 5 Hz frequency and 1 mm vibrational amplitude, (h) the output voltage at 10 Hz frequency and same 1 mm vibrational amplitude, and (i) the output voltage at 10 Hz frequency and 1 mm vibrational amplitude for up to 1000 cycles.

modulation. Figure 5b presents the *I–t* response under 565 nm illumination at 0.5 V bias upon bending. A clear modulation of current is observed with light on–off cycles, a dark current of ~20 nA, and increasing to 40 nA under illumination. The inset shows the corresponding response at the without bending flat state (0% strain) of the sample under the same applied bias and illumination light conditions, where no change in photocurrent is observed, highlighting the role of strain-induced piezoelectric polarization. Similarly, Figure 5c depicts the *I–t* response at a 660 nm illumination wavelength and a 0.5 V bias, revealing a photocurrent of ~10 nA, which is half that of the 565 nm wavelength, and no photoresponse under flat conditions under 660 nm can be seen in the inset. At an external applied bias of 1 V (inset of Figure 5d), the dark current is enhanced by 2.75-fold and reaches ~55 nA, likely due to the induced electric field surrounding the conductive channel, facilitating higher photogenerated charge carriers at applied higher bias. Thus, the observed currents under light illumination at 1 V bias are found to be 97 and 80 nA under the 565 nm (Figure 5d) and the 660 nm (Figure 5e), respectively. All unstrained measurements under the same optical and electrical conditions yielded negligible photocurrent, reinforcing the conclusion that the piezoelectric field under strain is essential for exciton dissociation and carrier separation. Figure 5f summarizes the extracted photocurrent values and light-to-dark-current ratios (LDCRs) for the different light illumination conditions under bending (at 1.2% strain). The photocurrent values were 20, 10, 42, and 25 nA for 565 nm at 0.5 V, 660 nm at 0.5 V, 565 nm at 1 V, and 660 nm at 1 V, respectively, corresponding to Figure 5b–e. The LDCRs were calculated as 2.0, 1.5, 1.76, and 1.45 for these respective conditions. Additionally, *I–t* measurements were conducted at a low light illumination intensity of 2 mW/cm^2 under similar applied bias conditions, depicted in Figure S8. Earlier, Wu et al. have made a flexible phototransistor based on a MoS2 monolayer and demonstrated piezo-optoelectronic coupling [25]. Their photoresponse was decreased on tensile strain, which contradicts their theoretical calculation. Our results

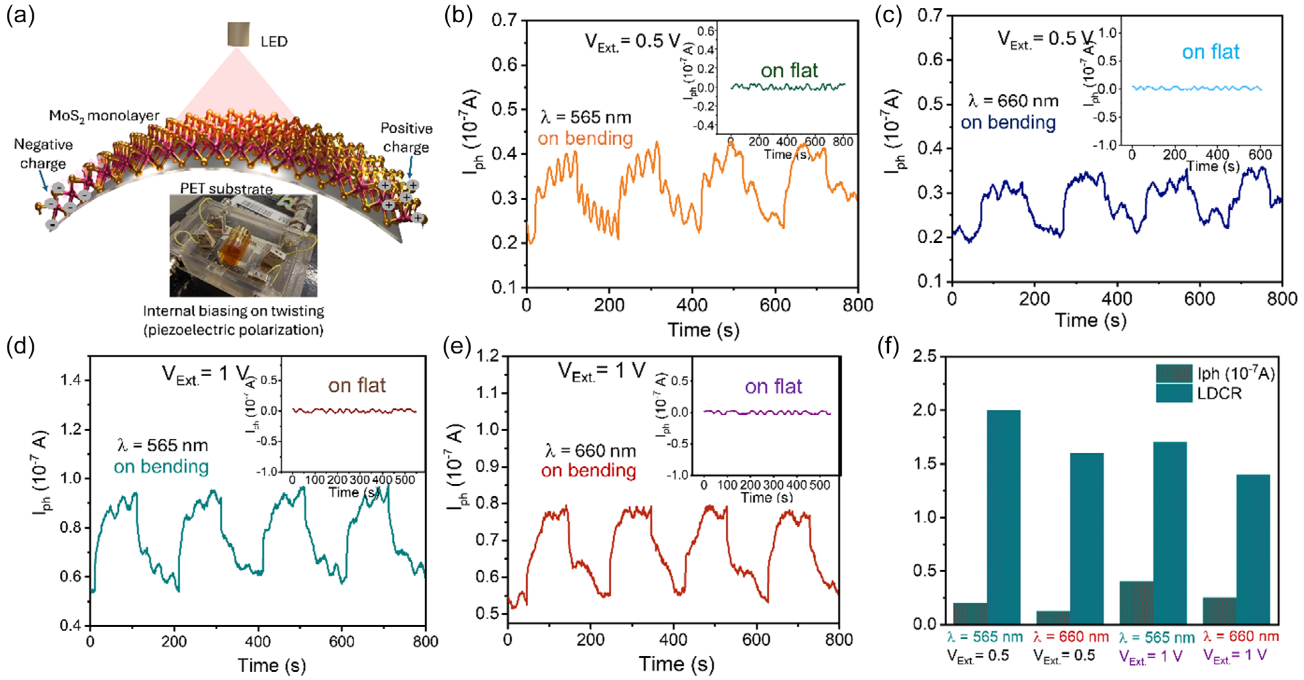

FIGURE 5 | Optoelectronic measurements of developed flexible device based on monolayer MoS$_2$. (a) Schematic of measurement setup and occurring phenomenon on bending (strained) MoS$_2$ flexible device. (b–e) External voltage and wavelength-dependent *I*–*t* measurement for monolayer MoS$_2$-based device under the light intensity of 20 mW/cm^2 (b) at external voltage of 0.5 V and wavelength of 565 nm under bending condition, (c) at external voltage of 0.5 V and wavelength of 660 nm under bending condition, (d) at external voltage of 1 V and wavelength of 565 nm under bending condition, (e) and at external voltage of 1 V and wavelength of 660 nm under bending condition. At the bending condition, the generated strain in the monolayer MoS$_2$ was 1.2%, while data under the flat condition, where no strain was introduced, is shown in the inset of the corresponding figure. (f) Achieved photocurrent and LDCR for all four conditions.

are consistent with theoretical expectations and the predicted enhancement in light absorption and carrier separation efficiency. This consistency reinforces the robustness and reliability of our experimental observations. Furthermore, we have shown the multifunction capability of energy generation, sensing, and photodetection within a single device.

To verify the stability of piezo-optoelectronic coupling, the photoresponse was further tested after 50 and 100 bending cycles at ~1.2% strain, shown in Figure S9. The results revealed negligible degradation in performance, underscoring the mechanical robustness and reproducibility of the coupling effect.

Collectively, these findings demonstrate that monolayer MoS$_2$ exhibits strain-driven piezo-optoelectronic coupling that enables efficient photocurrent generation at low operating voltages. The integration of energy generation, sensing, and photodetection within a single flexible configuration positions this material system as a promising platform for next-generation wearable multifunctional devices.

3 | Conclusions

In summary, we have provided the direct experimental demonstration of strain-driven piezo-optoelectronic coupling in large-area monolayer MoS$_2$. By correlating nanoscale piezoresponse with device-level photocurrent generation, we show that mechanical deformation can be harnessed as an effective control knob for light–matter interactions in atomically thin semiconductors. The measured out-of-plane piezoelectric coefficient ($d_{33}^{\mathrm{eff}} = 0.64$ pm/V) and the pronounced strain-induced enhancement of photocurrent confirm that internal polarization fields arising from lattice deformation play a decisive role in exciton dissociation and charge separation.

These findings advance the fundamental understanding of coupled electromechanical and optoelectronic phenomena in 2D materials, while also establishing monolayer MoS$_2$ as a multifunctional, scalable, and flexible platform for next-generation device technologies. Beyond proof-of-concept demonstrations, this work lays the foundation for developing mechanically programmable optoelectronics, hybrid sensors, and self-powered wearable technologies, where strain engineering provides a versatile pathway to tune device performance.

4 | Methods

4.1 | MoS$_2$ Monolayer Synthesis

Monolayer MoS$_2$ was synthesized via low pressure chemical vapor deposition (LPCVD) in a dual-zone tube furnace under two at low-pressure conditions [47]. Before growth, 300 nm SiO$_2$/Si substrates were cleaned in acetone by ultrasonic technique, then passed through isopropanol, deionized water, and finally dried by nitrogen. MoO$_3$ (20 mg), as Mo precursor, was placed along with the growth substrates in zone 2 of the furnace under a 500 sccm Ar flow for 10 min. Sulfur powder (200 mg) was placed upstream in zone 1 and heated to 180°C to generate S vapor, which was carried through to zone 2 by a 70 sccm

26884062, 2026, 1, Downloaded from https://onlinelibrary.wiley.com/doi/10.1002/sstr.202500657, Wiley Online Library on [12/02/2026]. See the Terms and Conditions (https://onlinelibrary.wiley.com/terms-and-conditions) on Wiley Online Library for rules of use; OA articles are governed by the applicable Creative Commons License

Ar flow as carrier gas, which was held at 750°C for 20 min of growth while maintaining low pressure (1 Torr). After the growth, the furnace was cooled under the flow of 500 sccm Ar.

4.2 | Material Characterizations

The optical image of the as-grown monolayer crystal was captured using a Leica microscope. AFM and surface potential mapping were performed using an MFP-Infinity system (Oxford Instruments, Asylum Research, United States) in ScanAsyst mode at a resolution of 256 × 256 pixels. Topographic and depth profiles were analyzed using Gwyddion software. Raman spectra were acquired using a Horiba Scientific LabRAM HR Evolution Raman spectrometer with a 532 nm laser and 1800 lines/mm grating. HR-TEM imaging was carried out using a JEOL JEM-F200 CFEG microscope operated at 200 kV.

XPS was performed using a Kratos AXIS Supra system equipped with a monochromatic Al Kα source (1486.7 eV). Data processing and peak deconvolution were conducted using CasaXPS software. SKPFM was utilized to evaluate the local surface potential, using PtIr-coated Si cantilevers (SCM-PIT-V2, Bruker; spring constant = 3 N/m, resonance frequency = 75 kHz). Tip work function was calibrated relative to a gold substrate ($\Phi = 5.1$ eV) [32]. Conducting force microscopy was performed on MoS_2 monolayers transferred to Au substrates using the same AFM system.

FET measurements were carried out using a back-gated geometry after polymer-assisted transfer of MoS_2 onto SiO_2/Si substrates. Electrical characterization was conducted using a Keithley 4200A-SCS Parameter Analyzer on a Signatone probe station. Photoresponse was recorded under dark and illuminated conditions using an Agilent 2912A source meter and monochromatic LEDs (Thorlabs) at 565 and 660 nm.

4.3 | Piezoelectric Measurements

Out-of-plane piezoelectric properties were measured using DART-PFM mode on a Cypher ES AFM system (Oxford Instruments, Asylum Research, United States). Data was collected using PtIr-coated stiff cantilevers (NanoWorld, spring constant = 42 N/m, length = 160 μm) to minimize electrostatic artifacts. The inverse optical lever sensitivity was calibrated using force-distance curves in contact mode [48]. A lock-in amplifier was utilized to determine the amplitude and phase signals under AC drive voltages ranging from 0 to 4 V, with a fixed resonance frequency. To suppress electrostatic effects, a DC tip bias equal to the surface potential was applied during measurements [16, 49]. Detailed information about the measurement of PFM data is shown in our earlier study [11].

4.4 | PED Fabrication and Testing

Flexible piezoelectric energy devices were fabricated using CVD-grown monolayer MoS_2. A PMMA-assisted wet transfer method was used to transfer the monolayers onto PET substrates, followed by PMMA removal with acetone. Cr/Pd/Au (1/20/50 nm) interdigitated electrodes were deposited using an E-beam evaporator (PVD75, Kurt J. Lesker), with a gap spacing of 100 μm and a length of 7 mm (Figure S3). A ~0.3-mm-thick PDMS encapsulation layer was added for mechanical protection and uniform stress distribution during testing.

Author Contributions

Ajay Kumar Verma: data curation (lead), methodology (lead) validation (lead), visualization (lead), writing – original draft (lead). **Pargam Vashishtha:** data curation (supporting), formal analysis (supporting), methodology (supporting). **Vishnu Aggarwal:** data curation (supporting), formal analysis (supporting). **Boopathiraja Kanan:** data curation (supporting), investigation (supporting). **Sindhu P. Giridhar:** investigation (supporting), methodology (supporting), validation (supporting). **Tanish Gupta:** methodology (supporting), visualization (supporting). **Md. Ataur Rahman:** methodology (supporting), writing – review and editing (supporting). **Manoj Sehrawat:** visualization (equal). **Chenglong Xu:** data curation (supporting), visualization (supporting). **Billy J. Murdoch:** visualization (supporting), validation (supporting). **Edwin LH Mayes:** formal analysis (supporting), visualization (supporting). **S. R. Dhakate:** supervision (supporting), writing – review and editing (supporting). **Bhasker Gahtori:** supervision (supporting), writing – review and editing (supporting). **Taimur Ahmed:** validation (supporting), writing – review and editing (supporting). **Irfan H. Abidi:** conceptualization (equal), funding acquisition (supporting). methodology (equal), project administration (supporting), supervision (equal), writing – original draft (supporting), writing – review and editing (equal). **Sumeet Walia:** conceptualization (equal), funding acquisition (lead), project administration (equal), resources (lead), supervision (lead), writing – review and editing (equal).

Acknowledgments

This research was conducted partly at the Micro Nano Research Facility (MNRF) at RMIT University, within Victoria's Australian National Fabrication Facility. We thank the MNRF and RMIT Microscopy and Microanalysis Research Facility staff for their technical assistance. S.W. and I.H.A. acknowledge support from the Australian Research Council Discovery Project DP220100020 and DP240100145. A.K.V. expresses gratitude to RMIT for financial support through the RMIT-AcSIR fellowship. S.P.G. acknowledges scholarship support through the National Intelligence and Security Research Grant (NS210100083) and the Department of Defence Science and Technology. S.W. and T.A. acknowledge support from the Office of National Intelligence (NI230100026). A.K.V. also acknowledges the Director of CSIR-NPL and AcSIR India for their enduring support.

Conflicts of Interest

The authors declare no conflicts of interest.

Data Availability Statement

The data that support the findings of this study are available from the corresponding author upon reasonable request.

References

1. J. Liu, Z. Li, S. Tian, et al., "A Magnetostrictive-Actuated Bionic Piezo-Phototronic Device for Dual-Threshold Adaptive Vision System," *Advanced Functional Materials*. (2025): e16899, https://doi.org/10.1002/adfm.202516899.

2. W. Wu and Z. L. Wang, "Piezotronics and Piezo-Phototronics for Adaptive Electronics and Optoelectronics," *Nature Reviews Materials* 1, no. 7 (2016): 1–17.

3. S. Manzeli, A. Allain, A. Ghadimi, and A. Kis, "Piezoresistivity and Strain-Induced Band Gap Tuning in Atomically Thin MoS2," *Nano Letters* 15, no. 8 (2015): 5330–5335.

26884062, 2026, 1, Downloaded from https://onlinelibrary.wiley.com/doi/10.1002/sstr.202500657, Wiley Online Library on [12/02/2026]. See the Terms and Conditions (https://onlinelibrary.wiley.com/terms-and-conditions) on Wiley Online Library for rules of use; OA articles are governed by the applicable Creative Commons License

4. Z. L. Wang and W. Wu, “Piezotronics and Piezo-Phototronics: Fundamentals and Applications,” *National Science Review* 1, no. 1 (2014): 62–90.

5. C. Tan, X. Cao, X.-J. Wu, et al., “Recent Advances in Ultrathin Two-Dimensional Nanomaterials,” *Chemical Reviews* 117, no. 9 (2017): 6225–6331.

6. K. S. Novoselov, A. Mishchenko, A. Carvalho, and A. Castro Neto, “2D Materials and Van der Waals Heterostructures,” *Science* 353, 6298 (2016): aac9439.

7. C. Cui, F. Xue, W.-J. Hu, and L.-J. Li, “Two-Dimensional Materials with Piezoelectric and Ferroelectric Functionalities., *npj 2D Materials and Applications* 2, no. 1 (2018): 18.

8. J. Lu, J. Yao, J. Yan, et al., “Strain Engineering Coupled with Optical Regulation towards a High-Sensitivity In 2 S. 3 Photodetector.,” *Materials Horizons* 7, no. 5 (2020): 1427–1435.

9. H. Qiu, T. Xu, Z. Wang, et al., “Hopping Transport through Defect-Induced Localized States in Molybdenum Disulphide,” *Nature Communications* 4, no. 1 (2013): 2642.

10. Y. S. Jung, H. J. Choi, S. H. Park, D. Kim, S.-H. Park, and Y. S. Cho, “Nanoampere-Level Piezoelectric Energy Harvesting Performance of Lithography-Free Centimeter-Scale MoS2 Monolayer Film Generators,” *Small* 18, no. 24 (2022): 2200184, https://doi.org/10.1002/smll.202200184.

11. A. K. Verma, M. A. Rahman, P. Vashishtha, et al., “Oxygen-Passivated Sulfur Vacancies in Monolayer MoS2 for Enhanced Piezoelectricity,” *ACS Nano* 19, no. 3 (2025): 3478–3489, https://doi.org/10.1021/acsnano.4c13037.

12. S. Manzeli, D. Ovchinnikov, D. Pasquier, O. V. Yazyev, and A. Kis, “2D Transition Metal Dichalcogenides,” *Nature Reviews Materials* 2, no. 8 (2017): 1–15.

13. Z. Wei, B. Li, C. Xia, et al., “Various Structures of 2D Transition-Metal Dichalcogenides and Their Applications,” *Small Methods* 2, no. 11 (2018): 1800094.

14. B. Radatovic, O. Çakıroğlu, V. Jadrisko, et al., “Strain-Enhanced Large-Area Monolayer MoS2 Photodetectors,” *ACS Applied Materials & Interfaces* 16, no. 12 (2024): 15596–15604.

15. W. Wu, L. Wang, Y. Li, et al., “Piezoelectricity of Single-Atomic-Layer MoS2 for Energy Conversion and Piezotronics,” *Nature* 514, no. 7523 (2014): 470–474.

16. L. Collins, Y. Liu, O. S. Ovchinnikova, and R. Proksch, “Quantitative Electromechanical Atomic Force Microscopy,” *ACS Nano* 13, no. 7 (2019): 8055–8066.

17. B. J. Rodriguez, C. Callahan, S. V. Kalinin, and R. Proksch, “Dual-Frequency Resonance-Tracking Atomic Force Microscopy,” *Nanotechnology* 18, no. 47 (2007): 475504.

18. H. Zhu, Y. Wang, J. Xiao, et al., “Observation of Piezoelectricity in Free-Standing Monolayer MoS2,” *Nature Nanotechnology* 10, no. 2 (2015): 151–155.

19. D. Lu, Y. Chen, L. Kong, et al., “Strain-Plasmonic Coupled Broadband Photodetector Based on Monolayer MoS2,” *Small* 18, no. 14 (2022): 2107104.

20. C. J. Brennan, R. Ghosh, K. Koul, S. K. Banerjee, N. Lu, and E. T. Yu, “Out-of-Plane Electromechanical Response of Monolayer Molybdenum Disulfide Measured by Piezoresponse Force Microscopy,” *Nano Letters* 17, no. 9 (2017): 5464–5471.

21. X. Lin, Z. Feng, Y. Xiong, et al., “Piezotronic Neuromorphic Devices: Principle, Manufacture, and Applications,” *International Journal of Extreme Manufacturing* 6, no. 3 (2024): 032011.https://doi.org/10.1088/2631-7990/ad339b.

22. Y. Wang, Q. Sun, and Z. L. Wang, “Piezotronics and Tribotronics of 2D Materials.,” *Materials Science and Engineering: R: Reports* 164 (2025): 100951, https://doi.org/10.1016/j.mser.2025.100951.

23. P. Gant, P. Huang, D. P. de Lara, D. Guo, R. Frisenda, and A. Castellanos-Gomez, “A Strain Tunable Single-Layer MoS2 Photodetector,” *Materials Today* 27 (2019): 8–13.

24. J. Du, H. Yu, B. Liu, et al., “Strain Engineering in 2D Material-Based Flexible Optoelectronics,” *Small Methods* 5, no. 1 (2021): 2000919.

25. W. Wu, L. Wang, R. Yu, et al., “Piezophototronic Effect in Single-Atomic-Layer MoS2 for Strain-Gated Flexible Optoelectronics,” *Advanced Materials* 28, no. 38 (2016): 8463–8468.

26. W. Chen, J. Zhao, J. Zhang, et al., “Oxygen-Assisted Chemical Vapor Deposition Growth of Large Single-Crystal and High-Quality Monolayer MoS2,” *Journal of the American Chemical Society* 137, no. 50 (2015): 15632–15635.

27. T. Yanase, F. Uehara, I. Naito, T. Nagahama, and T. Shimada, “Healing Sulfur Vacancies in Monolayer MoS2 by High-Pressure Sulfur and Selenium Annealing: Implication for High-Performance Transistors,” *ACS Applied Nano Materials* 3, no. 10 (2020): 10462–10469.

28. Y. Zhu, J. Lim, Z. Zhang, et al., “Room-Temperature Photoluminescence Mediated by Sulfur Vacancies in 2D Molybdenum Disulfide,” *ACS Nano* 17, no. 14 (2023): 13545–13553.

29. S. A. Han, T. H. Kim, S. K. Kim, et al., “Point-Defect-Passivated MoS2 Nanosheet-Based High Performance Piezoelectric Nanogenerator,” *Advanced Materials* 30, no. 21 (2018): 1800342.

30. I. S. Kim, V. K. Sangwan, D. Jariwala, et al., “Influence of Stoichiometry on the Optical and Electrical Properties of Chemical Vapor Deposition Derived MoS2,” *ACS Nano* 8, no. 10 (2014): 10551–10558.

31. P.-C. Shen, Y. Lin, C. Su, et al., “Healing of Donor Defect States in Monolayer Molybdenum Disulfide Using Oxygen-Incorporated Chemical Vapour Deposition,” *Nature Electronics* 5, no. 1 (2022): 28–36.

32. W. Melitz, J. Shen, A. C. Kummel, and S. Lee, “Kelvin Probe Force Microscopy and Its Application,” *Surface Science Reports* 66, no. 1 (2011): 1–27.

33. P. Vashishtha, C. Kofler, A. K. Verma, et al., “Epitaxial Interface-Driven Photoresponse Enhancement in Monolayer WS2–MoS2 Lateral Heterostructures,” *Advanced Functional Materials*. (2025): e12962, https://doi.org/10.1002/adfm.202512962.

34. P. Ramaswamy, S. Devkota, R. Pokharel, et al., “A Study of Dopant Incorporation in Te-Doped GaAsSb Nanowires Using a Combination of XPS/UPS, and C-AFM/SKPM,” *Scientific Reports* 11, no. 1 (2021):8329,

35. Z. Zhang, G. Yu, J. Garcia-Barriocanal, Z. Xie, and C. D. Frisbie, “Strain–Work Function Relationship in Single-Crystal Tetracene,” *ACS Applied Materials & Interfaces* 12, no. 36 (2020): 40607–40612.

36. K. Cho, M. Min, T.-Y. Kim, et al., W.-K. Electrical and Optical Characterization of MoS2 with Sulfur Vacancy Passivation by Treatment with Alkanethiol Molecules,” *ACS Nano* 9, no. 8 (2015): 8044–8053.

37. D. M. Sim, M. Kim, S. Yim, et al., “Controlled Doping of Vacancy-Containing Few-Layer MoS2 via Highly Stable Thiol-Based Molecular Chemisorption,” *ACS Nano* 9, no. 12 (2015): 12115–12123.

38. A. Ortiz-Conde, F. J. García-Sánchez, J. Muci, A. T. Barrios, J. J. Liou, and C.-S. Ho, “Revisiting MOSFET Threshold Voltage Extraction Methods.,” *Microelectronics Reliability* 53, no. 1 (2013): 90–104.

39. V. Aggarwal, I. H. Abidi, J. Limb, et al., “Stacking Mode-Driven Enhancement of Optoelectronic and Electrocatalytic Properties in Bilayer 2H MoS2,” *ACS Applied Materials & Interfaces* 17, no. 34 (2025): 48658–48669.

40. X. Wang, X. He, H. Zhu, et al., “Subatomic Deformation Driven by Vertical Piezoelectricity from CdS Ultrathin Films,” *Science Advances* 2, no. 7 (2016): e1600209.

41. R. Proksch, R. Wagner, and J. Lefever, “Accurate Vertical Nanoelectromechanical Measurements,” *Journal of Applied Physics* 135, no. 3 (2024): 035104.

42. L. Gu, J. Liu, N. Cui, et al., “Enhancing the Current Density of a Piezoelectric Nanogenerator Using a Three-Dimensional Intercalation Electrode,” *Nature Communications* 11, no. 1 (2020): 1030.

26884062, 2026, 1, Downloaded from https://onlinelibrary.wiley.com/doi/10.1002/sstr.202500657, Wiley Online Library on [12/02/2026]. See the Terms and Conditions (https://onlinelibrary.wiley.com/terms-and-conditions) on Wiley Online Library for rules of use; OA articles are governed by the applicable Creative Commons License

43. A. Sohn, H. J. Hwang, P. Zhao, et al., "Boosting the Output Performance of the MoS2 Monolayer-Based Piezoelectric Nanogenerator by Artificial Dual Strain Concentration," *ACS Applied Materials & Interfaces* 16, no. 1 (2023): 1317–1325.

44. S. A. Han, T.-H. Kim, S. K. Kim, et al., "Point-Defect-Passivated MoS2 Nanosheet-Based High Performance Piezoelectric Nanogenerator." *Advanced Materials* 30, no. 21 (2018): 1800342, https://doi.org/10.1002/adma.201800342.

45. Y. Kang, S. Pyo, E. Jo, and J. Kim, "Light-Assisted Recovery of Reacted MoS2 for Reversible NO2 Sensing at Room Temperature," *Nanotechnology* 30, no. 35 (2019): 355504, https://doi.org/10.1088/1361-6528/ab2277.

46. Y. Wang, F. Li, W. Peng, W. Xie, X. Zhao, and Y. He, "Flexible Phototransistor Array Enhanced by Coupling the Piezo-Phototronic Effect and the Flexoelectric Effect for Strain/Optical Sensing and Imaging," *Advanced Materials Technologies* 10, no. 3 (2025): 2400939.

47. I. H. Abidi, S. P. Giridhar, J. O. Tollerud, et al., "Oxygen Driven Defect Engineering of Monolayer MoS_2 for Tunable Electronic, Optoelectronic, and Electrochemical Devices." *Advanced Functional Materials* 37, no. 34 (2024): 2402402, https://doi.org/10.1002/adfm.202402402.

48. N. Balke, S. Jesse, P. Yu, B. Carmichael, S. V. Kalinin, and A. Tselev, "Quantification of Surface Displacements and Electromechanical Phenomena via Dynamic Atomic Force Microscopy," *Nanotechnology* 27, no. 42 (2016): 425707.

49. S. Bradler, A. Schirmeisen, and B. Roling, "Amplitude Quantification in Contact-Resonance-Based Voltage-Modulated Force Spectroscopy," *Journal of Applied Physics* 122, no. 6 (2017): 065106.

Supporting Information

Additional supporting information can be found online in the Supporting Information section. **Supporting Fig. S1:** XPS elemental mapping for Mo 3d state and the survey spectra of the MoS_2 monolayer crystal. **Supporting Fig. S2:** PFM phase map of MoS_2 monolayer crystal with different AC drive voltages (a) at 0 V, (b) at 1 V, (c) at 2 V, (d) at 3 V, and (e) at 4 V. **Supporting Fig. S3:** PED fabrication process using large-area monolayer MoS_2 crystal. (a) As-grown MoS_2 monolayer on SiO_2 substrate. (b) Then PMMA polymer spin-coating over the MoS_2 monolayers. (c) The MoS_2 flakes were peeled off with PMMA and transferred on flexible PET substrate. (d) Polymer PPMA was removed by acetone wash. (e) The interdigital patterns were designed on the MoS_2 flakes and then electrodes of Au/Cr were deposited there in a designed pattern; here, the gap between electrodes is 100 μm. (f) PDMS coating on this device to protect with unwanted damage. **Supporting Fig. S4:** (a) PED with no in-plane strain when no tapping. (b) Upon tapping, an in-plane strain occurs and generates piezoelectric polarization. **Supporting Fig. S5:** (a) Blank device testing for voltage generation, MoS_2 monolayer is missing under electrodes, to confirm the response in other devices is coming from MoS_2 crystal, (b) the rectified output voltage upon finger tapping using a full wave bridge rectifier, (c) the generated output voltage across 2.2 MΩ by the PED on finger tapping, and (d) the 1 μF capacitor charging by the MoS_2 PED upon finger tapping. **Supporting Fig. S6:** The electromechanical performance of PED based on MoS_2 monolayer. (a) The schematic of the mechanical vibrating setup, (b) actual setup utilized for the measurements, (c) the generated output voltage by the PED at 2 Hz and under 1 mm vibrational amplitude, (d) the output voltage at 2 Hz and under 1 mm vibrational amplitude up to 200 cycles, and (e) the output voltage at 5 Hz and under 1 mm vibrational amplitude up to 500 cycles. **Supporting Fig. S7:** The schematic of mechanism behind the strain induced piezoelectric effect supports photoresponse. (a) Case 1: when metal contacts are not connected to MoS_2, Fermi levels are not aligned. (b) Case 2: when metal contacts are connected to MoS_2 but no strain is applied, Fermi levels will align and will create a barrier height. (c) Case 3: when metal contacts are connected to MoS_2 and strain is applied, the internal piezoelectric polarization supports the electron–hole pair separation. **Supporting Fig. S8:** The external voltage and wavelength-dependent I–t measurement for MoS_2 monolayer-based device under the light intensity of 2 mW/cm^2; (a) at external voltage of 0.5 V and wavelength of 565 nm under bending condition, (b) at external voltage of 0.5 V and wavelength of 660 nm under bending condition, (c) at external voltage of 1 V and wavelength of 565 nm under bending condition, (d) and at external voltage 1 V and wavelength of 660 nm under bending condition. At the bending condition, the generated strain in the MoS_2 monolayer was 1.2%, while data under the flat condition, where no strain was introduced, is shown in the inset of the corresponding figure. **Supporting Fig. S9:** The stability test for optoelectronic coupling after bending cycles; the I–t measurement for MoS_2 monolayer-based device under the light intensity of 20 mW/cm^2, at external voltage of 1 V and wavelength of 565 nm, (a) after 50 bending cycles and (b) after 100 bending cycles. The bending cycles were performed manually between 0% and 1.2% strain, while data under the flat condition, where no strain was introduced, is shown as inset of respective subfigure. **Supporting Table S1:** The comparison of performance parameters of the MoS_2 monolayer-based flexible photodetector.

Biographies

Ajay Kumar Verma holds dual Ph.D.: one in engineering from RMIT University, Australia, and another in physical sciences from AcSIR, India. He has worked on flexible thermoelectrics at Karlsruhe Institute of Technology, Germany, as a postdoctoral researcher. His research focuses on piezoelectric and thermoelectric materials and their technological applications. He has expertise in surface characterisations using scanning probe microscopy.

Pargam Vashishtha holds dual Ph.D.: one in engineering from RMIT University, Australia, and another in physical sciences from AcSIR, India. He is currently a research associate at the University of Wisconsin-Madison, United States, where his research focuses on the fabrication of grafted UWBG material heterostructures for power electronics. His expertise covers the fabrication and band engineering of a full range of inorganic heterostructures, 2D/2D, 2D/3D, and 3D/3D design for electronic devices.

Vishnu Aggarwal earned his doctoral degree in March 2025 under the AcSIR-RMIT University cotutelle Ph.D. program. His doctoral research broadly focused on the development of self-powered and broadband photodetectors. He is currently a postdoctoral researcher contributing to cross-disciplinary projects on piezoelectric paint based sensors and on the fabrication of SWIR sensors.

Boopathiraja Kanan completed a master of engineering by research in electrical and electronics engineering at RMIT University. His research experience includes electrochemical and optoelectronic sensors, 2D material–based electrochemical reaction studies. He has expertise in photolithography and nanofabrication techniques for device development.

Sindhu P. Giridhar received their bachelor's and honours degrees in biomedical engineering and is currently a final-year Ph.D. candidate in electronic engineering at RMIT University, Australia. Their research focuses on interface engineering of 2D chalcogenides for optoelectronic and electronic applications. They have published in peer-reviewed journals on 2D material synthesis, device physics, and characterization. In addition to their doctoral research, they have experience in microfabrication of electronic devices for a project with the Department of Defence Science and Technology.

26884062, 2026, 1, Downloaded from https://onlinelibrary.wiley.com/doi/10.1002/sstr.202500657, Wiley Online Library on [12/02/2026]. See the Terms and Conditions (https://onlinelibrary.wiley.com/terms-and-conditions) on Wiley Online Library for rules of use; OA articles are governed by the applicable Creative Commons License

Tanish Gupta is pursuing his doctoral studies in the School of Electrical and Electronic Engineering at RMIT University, Melbourne, Australia. His research focuses on the synthesis and characterization of transition metal dichalcogenides, with applications in optoelectronic devices.

Md. Ataur Rahman is an electronic materials engineer specializing in translating laboratory research into industry through prototyping and engineering wearable sensors for biosignals, airborne viruses, harmful gases, and skin-like electronics. He holds a B.S. from Chittagong University of Engineering and Technology, an M.S. from the University of Ulsan, and a Ph.D. from RMIT University. He has received the Jack Brockhoff Early Career Medical Research Grant (2022), Heart Foundation Postdoctoral Fellowship (2023), and ARC Early Career Industry Fellowship (2024). He has over 40 publications, secured $3.7 million in research income, and is a Senior Lecturer at RMIT University.

Manoj Sehrawat received his Ph.D. through the AcSIR-RMIT Joint Programme in 2025, specializing in 1D/2D nanomaterials and structural composites. Now an R&D industrial chemist, he focuses on the design and application of advanced wear-resistant materials for leading-edge manufacturing.

Chenglong Xu received his Ph.D. in chemical and biomolecular engineering from the University of Melbourne. He is currently a senior technical officer at the RMIT Micro Nano Research Facility (MNRF). His expertise includes micro/nano fabrication and advanced material characterization.

Billy J. Murdoch received his Ph.D. in physics at RMIT University in 2016. He has previously worked as a Research Associate at the National EPSRC XPS Users Service (NEXUS) at Newcastle University, UK and postdoctoral research fellow at RMIT University. He is currently a senior technical officer in the RMIT microscopy & microanalysis facility. His areas of expertise are electron microscopy, X-ray photoelectron spectroscopy, vacuum thin film deposition, & neuromorphic computing.

Edwin L. H. Mayes attained his Ph.D. in physics at RMIT in 2015. Has worked as a TEM manager at RMIT. Now employed as a senior technical officer in the RMIT microscopy and microanalysis facility. Expert in transmission electron microscopy and related techniques. Specialised in in-situ TEM analysis. Experience with thin film deposition, device fabrication.

S. R. Dhakate received his Ph.D. in physics from the University of Delhi, India. He is currently as chief scientist and professor at CSIR-National Physical Laboratory, New Delhi, India. His expertise is in the area of advanced materials, particularly carbon-based materials. He has published more than 275 research articles in reputed journals and serval patents in his credit.

Bhasker Gahtori received his Ph.D. in physics from Jamia Millia Islamia, University, New Delhi, India. At present, he is a senior principal scientist at CSIR–National Physical Laboratory (NPL), New Delhi, India. His work significantly contributes to the development of alternative energy solutions through innovative materials research, particularly in the field of thermoelectrics.

Taimur Ahmed received his Ph.D. from RMIT University, Australia, in 2018. His research focuses on low dimensional materials and bio-inspired optoelectronic nanodevices for next-generation electronics. He has pioneered neuromorphic memories and multifunctional devices that integrate electrical, optical, and mechanical functionalities at the nanoscale. His work broadly advances the use of low-dimensional material platforms for flexible, multifunctional and energy-efficient sensing and computing technologies.

Irfan H. Abidi received the Ph.D. in chemical and biomolecular engineering (nanotechnology) from the Hong Kong University of Science and Technology (HKUST), Hong Kong, in 2018. From 2018 to 2021, he was a research fellow with the Centre for Advanced 2D Materials, National University of Singapore, a world-leading graphene research center. He is currently a research fellow with the School of Engineering, RMIT University, Melbourne, VIC, Australia. His research focuses on engineering atomic structures in 2D materials from single crystalline to amorphous phases, using chemical vapor deposition (CVD) and laser-CVD techniques for applications in optoelectronics, quantum technologies, energy storage, and electrochemical devices. His work bridges fundamental science and applied research, addressing key industrial challenges through strong collaborations with national and international academic and industry partners.

Sumeet Walia is currently a professor and the director of RMIT's Centre for Opto-electronic Materials and Sensors (COMAS). His research focuses on discovering and manipulating fundamental properties of materials for applications across energy, nano/optoelectronics, sensors, and healthcare. He has coauthored more than 170 peer reviewed publications, including authoritative reviews in prestigious journals, is a named inventor on 15 patents and editor of two books for the CRC Press. He partners with several cross-sector industries to translate fundamental discoveries into the real world. He is also an avid contributor in enhancing equity, diversity, inclusion, and access in STEM. He chaired the national equity, diversity, and inclusion committee of Science and Technology Australia and has been part of advisory boards of the Victorian government and the Australian Academy of Technology and Engineering. His scientific and leadership contributions have been recognised through several national and international awards, including the Eureka Prize for Science leadership and the MIT Technology Review's Top 10 Innovators in APAC.

26884062, 2026, 1, Downloaded from https://onlinelibrary.wiley.com/doi/10.1002/sstr.202500657, Wiley Online Library on [12/02/2026]. See the Terms and Conditions (https://onlinelibrary.wiley.com/terms-and-conditions) on Wiley Online Library for rules of use; OA articles are governed by the applicable Creative Commons License